ELSEVIER

Contents lists available at ScienceDirect

# **Mechanics of Materials**

journal homepage: www.elsevier.com/locate/mecmat



#### Editor invited article

# Computational homogenization of linear elastic properties in porous non-woven fibrous materials

Mikhail Kuts<sup>a</sup>, James Walker<sup>b</sup>, Pania Newell<sup>b,\*</sup>

- <sup>a</sup> Independent researcher, Russia
- <sup>b</sup> Department of Mechanical Engineering, The University of Utah, Salt Lake City, UT, USA

#### ARTICLE INFO

#### Keywords: Fibrous porous media Finite element modeling Mechanical properties FEniCSx

#### ABSTRACT

Porous non-woven fibrous media are widely used in various industrial applications such as filtration, insulation, and medical textiles due to their unique structural and functional properties. However, predicting the mechanical behavior of these materials is challenging due to their complex microstructure and anisotropic nature. In this study, a computational model is developed to simulate the mechanical response of porous non-woven fibrous media under external loading. The model is based on the finite element method and takes into account the geometric and material properties of the fibers and the void spaces between them. The effects of various factors such as fiber size, porosity, and fibers' intersection ratio on the mechanical behavior of the material are investigated. The results reveal that the material's porosity and fibers' intersection ratio are the most significant factors influencing its mechanical properties. Additionally, the increase in fiber diameter has a relatively minor effect on the material's elastic properties. However, such changes in elastic properties are primarily attributed to the increase in randomness within the fibrous network, which is directly related to the fiber diameter for the investigated structure. The proposed computational model predicts the mechanical properties of porous non-woven fibrous media and can provide invaluable insights into the design and optimization of porous non-woven fibrous media for various scientific and engineering applications.

## 1. Introduction

Fibrous porous materials, which consist of randomly distributed fibers in a network structure, have gained significant attention due to their wide range of applications in various engineering and scientific fields. Such materials possess unique properties that surpass those of the constituent fibers. These properties include high porosity, large surface area, and lightweight, which contribute to their high absorptive, filtration, and thermal and acoustic insulation capabilities (Liu et al., 2014; Yilmaz et al., 2020; Cheng et al., 2023). Additionally, some materials exhibit enhancement in their mechanical properties when the fiber diameter is less than 200 nm (Cheng et al., 2023). These unique functionalities led to their utilization in diverse areas including medical masks, filters, thermal and sound insulation, battery separators, absorbent products, and packaging materials.

Materials with randomly distributed fibers can be divided into two large classes, depending on their structure: quasi-structured and randomly distributed (Picu, 2011). The first class includes materials with a perturbed regular structure, such as quasi-body centered cubic nanolattices (Cheng et al., 2023) or the open-cell foams (see Fig. 1-a).

These materials exhibit significant similarities and can be considered as a unified class of materials. Materials with controlled fiber orientation obtained by electrostatic deposition and spinning or magnetic alignment of fibers also belong to this class. Other types of materials have a random distribution of fibers without any specific structure (see Fig. 1-b-d). But even in such materials, their fibers can have a predominant orientation along one or several axes or planes (see Fig. 1-c), such as the needle-punched structures, which are produced from non-woven fiber fabrics by means of a through-thickness needling technique (Chen et al., 2016; Dabirvan et al., 2018).

The structure of non-woven fibrous materials is mainly determined by the fiber material and the manufacturing process. Furthermore, there are different methods of fiber bonding including mechanical, chemical, and thermal bonding (Yilmaz et al., 2020). In chemical bonding, binding agents are used in combination with various methods such as spraying, printing, coating, or saturation to connect fibers together (see Fig. 1-a). The resulting medium is fully connected, where all fibers are bonded, and the fiber connections transmit both axial forces and moments. In thermal bonding, fibers are joined together

Invited Editor: Lori Graham-Brady.

\* Corresponding author.

E-mail address: pania.newell@utah.edu (P. Newell).

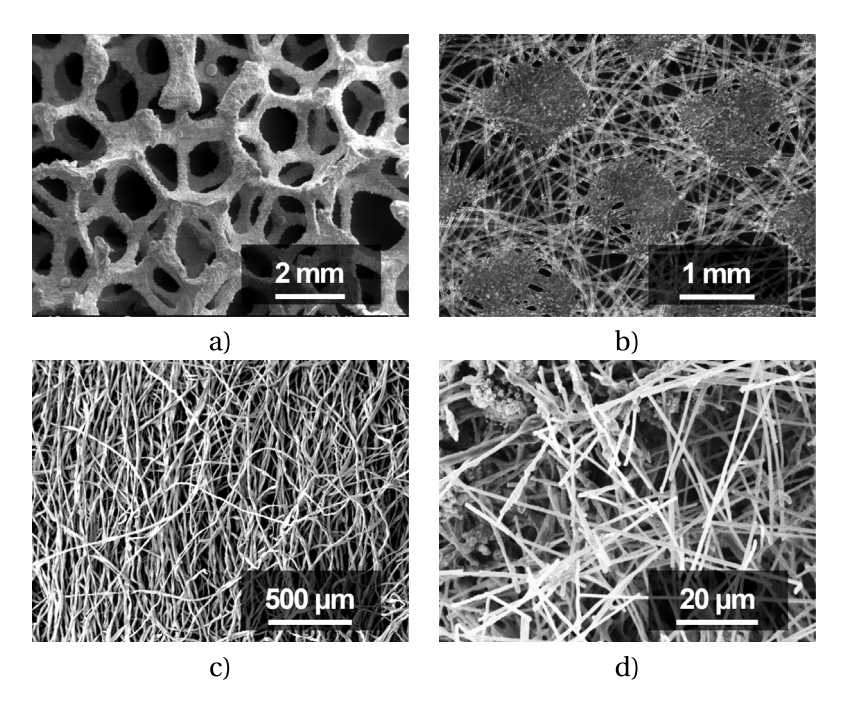


Fig. 1. SEM pictures of fibrous materials: a – Metal Foam in Scanning Electron Microscope ©SecretDisc, CC BY-SA 3.0; b – Outer Layer of Medical Mask ©Alexander Klepnev, CC BY 4.0; c – Cotton Fibers ©Janice Carr, Laura Rose, USCDCP, CC0; d – "Moonmilk" Calcium Carbohydrate Fibers ©Brian England, CC-BY-4.0.

through a heating and cooling process (see Fig. 1-c). However, the main method of fiber bonding is mechanical bonding (see Fig. 1-d), which involves fibers being bonded using methods such as hydroentanglement, stitching, and needle punching. Overall, due to the immense diversity in structure and available fabrication methods, designing fibrous porous materials with specific properties is a complex task.

Understanding the effective properties of fibrous porous materials is essential for gaining insights into their behavior and optimizing their performance. By determining the effective properties, we can comprehend how these materials behave under external loads. Moreover, understanding the effective properties allows us to assess the overall performance of existing fibrous porous materials, providing valuable information for quality control and ensuring reliable and efficient applications. In addition to understanding existing materials, knowledge of effective properties plays a significant role in the future design of fibrous porous materials. By manipulating and tailoring the material structural parameters, such as porosity, fiber diameter and shape, and method of fiber binding, we can engineer materials with desired effective properties. This enables the design of materials that exhibit specific mechanical strength, thermal conductivity, permeability, or other targeted characteristics. However, achieving this level of control requires the development of a robust computational model capable of accurately predicting the effective properties of fibrous porous materials and in our case mechanical properties of non-woven fibrous materials. This poses a challenge, as a model must account for the complex interplay between material behavior and various structural parameters.

Over the past decades, extensive research has been conducted on fibrous porous systems. An early contribution to the study of the mechanical properties of fibrous media is the work by Cox (Cox, 1952), where he obtained an analytical solution describing the deformations of a two-dimensional (2D) fibrous system. This work assumed that the fibers only experience tension while their orientation is random and described by a distribution function. In a series of recent works, Bosco et al. Bosco et al. (2015, 2016, 2017) developed analytical solutions for describing the hygro-mechanical behavior of fibrous porous systems. Their work focused on simplified 2D lattice structures with orthogonal fiber arrangements. In one of their studies (Bosco et al., 2017), they explored an analytical solution based on the Voigt model, where the fibrous medium is treated as a composite plate composed of an infinite

number of layers oriented according to a probability density function. However, they showed that such models have inherent limitations and are applicable only within a restricted range of coverage area and fiber orientations.

To address the limitations of analytical solutions, numerical models have been employed to investigate fibrous porous systems, offering more flexibility and the ability to consider a greater number of factors compared to analytical approaches. For instance, Farukh et al. Farukh et al. (2013) conducted an finite element analysis (FEA) of a thermally bonded non-woven fibrous system, incorporating damage criteria based on the deformation and fracture behavior of individual fibers into their model. Sozumer et al. Sozumert et al. (2015) also took a similar approach to investigate the effect of the central notch on non-woven fibrous networks experimentally and numerically. Additionally, it is also worth noting that there is a significant amount of works containing experimental investigations on the mechanical behavior of both individual fibers (Farukh et al., 2013) and fibrous systems (Sozumert et al., 2015; Cucumazzo et al., 2021). For instance, Cucumazzo et al. Cucumazzo et al. (2021) investigated the rate dependency of fibers by individually testing fibers that exhibited nonlinear elasticity followed by plastic strain hardening up to failure. These results were further incorporated in their paper (Cucumazzo and Silberschmidt, 2022) where they used an approach to model the mechanical behavior of a thermally bonded fibrous network using shell elements.

A more advanced approach has been proposed by Kulachenko and Uesaka in Kulachenko and Uesaka (2012) where they introduced a framework for direct modeling of 2D paperlike random fibrous networks, employing 3-node Timoshenko beam elements. Later Borodulina et al. Borodulina et al. (2012) utilized their framework to simulate fracture dynamics of a dry fiber network during tensile loading. In another work, Borodulina et al. Borodulina et al. (2018) investigated the effect of variation of individual fibers' and bonds' properties on the effective stiffness and strength of the fibrous network. The additional development of these works is demonstrated in the works of Mansur et al. Mansour et al. (2019), Mansour and Kulachenko (2022), where authors used the same framework as described in Kulachenko and Uesaka (2012), to develop a stochastic constitutive model for an isotropic fibrous network, transitioning from representative volume elements (RVE) to stochastic volume element (SVE). The proposed approach

enables the propagation of uncertainties from the microscale to the macroscale, allowing for more efficient modeling of the behavior of an isotropic fibrous network compared to directly simulating the entire medium. Other researchers (Lu et al., 2013; Liu et al., 2013, 2014) adopted a similar approach to model three-dimensional (3D) random fibrous (RF) networks composed of ceramics. Using 2-node Timoshenko beam elements, interfiber contact was simulated, incorporating the combined influences of grain boundaries and interfaces.

A drawback of using beam elements is the complexity of extending the model to investigate coupled thermo-hydro-mechanical (THM) behavior. Geers et al. Bosco et al. (2016, 2017), Samantray et al. (2022), Bosco et al. (2022) proposed a 2D framework for studying the THM behavior of paper-like materials represented as random fibrous networks. A regular grid with quadrilateral elements was used to construct the geometry. Although this approach allows for modeling the THM behavior of a wide range of fibrous materials (nonwoven, lattice, etc.), it has several limitations: 1) the usage of spatial discretization method results in a coarse representation of fiber boundaries and introduces dimensional redundancy in solving system of linear equations (SLE), causing higher computations compared to adaptive meshing; 2) this method is applicable only to materials with pronounced 2D structures: 3) the 2D description does not account for fibers wrapping each other (Bosco et al., 2022). Therefore, the most promising approach is to model fibrous materials in a 3D framework, as it allows for a more accurate consideration of the material's internal mechanics. However, currently, there is a scarcity of works utilizing a 3D framework to study random fibrous networks. One such work is (Veyhl et al., 2013), which investigates the mechanical behavior of sintered metallic fiber structures. In this study, the simulations are conducted based on actual material structures obtained from micro-computed tomography (micro-CT) images. The resulting model consists of over 4.5 million linear elements, which is computationally demanding.

Karakoc et al. Karakoc et al. (2020) also used a 3D finite element method (FEM) to examine 2D random fibrous networks composed of curvilinear fibers. They presented an original approach involving the projection of the fibers' boundary nodes onto the control nodes of the domain bounding the RVE, followed by solving a boundary value problem on this domain instead of the RVE boundary domain. Such an approach is highly suitable for investigating RVEs with nonconformal meshes, particularly for 2D networks such as paper. The main disadvantage of this work is the usage of elements with reduced integration, which resulted in a lower accuracy.

Additionally, it is worth mentioning that others (Rahali et al., 2016; Ganghoffer et al., 2020) also investigated the elastic behavior of woven materials with different structures (2D and 3D) in a 3D framework. These studies combine homogenization methods with the higher-order elasticity terms to determine the averaged components of the stiffness and curvature tensors, offering advantages when the scales separation approach does not apply (Vazic et al., 2022a). The drawbacks of these works include the use of a regular "Voxel" grid, which significantly increases the number of degrees of freedom in the problem, imprecise description of fiber boundaries, and the usage of elements with reduced integration, which exhibit low accuracy. Thus, it is crucial to develop a computationally efficient model that allows for the investigation of the behavior of random fibrous networks in a 3D framework.

Thus, it can be observed that the existing literature lacks comprehensive studies on the mechanical properties of non-woven fibrous materials in the context of 3D random fibrous networks. Most previous works have primarily focused on 2D structures or have utilized simplified fiber representations, which limit their ability to accurately capture the complex behavior of real-world non-woven materials. Moreover, the few studies that do consider 3D structures often examine ordered materials with significantly smaller RVEs. Motivated by these research gaps, the objective of this study is to develop a numerical model that accounts for various structural parameters, including porosity, fiber diameter, fiber shape, and the method of fiber binding. By investigating

the mechanical properties of non-woven fibrous materials in their true 3D complexity, this research aims to offer a more comprehensive understanding of their behavior, enabling the optimization of material construction and improvement of operational characteristics.

The paper is structured as follows: in Section 1, we provide an overview of the methodology, including the constitutive model, properties identification, and a detailed description of the computational workflow using the FEniCSx framework. Section 2 focuses on the model setup, encompassing the problem description, network geometry generation, numerical setup, and an in-depth analysis of mesh convergence. Section 3 presents and discusses the simulation results, and finally, Section 4 provides the concluding remarks for the paper.

#### 2. Methodology

In this section, we start with a brief overview of the constitutive model for fibrous systems followed by some general insights into the asymptotic homogenization method. Subsequently, we introduce the details of our computational workflow and the tools used in our study.

#### 2.1. Constitutive model and properties of fibrous network

In this study, we consider a fibrous porous network made of polypropylene (PP) fibers. PP can be considered as isotropic material, meaning that its mechanical properties are independent of the direction. This assumption simplifies the modeling process and allows for a more straightforward analysis of the fibrous network. The constitutive model used to describe the behavior of the fibrous network is given through the constitutive relation

$$\mathbf{\sigma} = {}^{4}\mathbf{C}^{f} : \mathbf{\varepsilon} \tag{1}$$

where  $\sigma$  is the Cauchy stress tensor,  $^4C^f$  is the 4th order elasticity tensor and  $\epsilon$  is the symmetric strain tensor. In Voigt notation, the elasticity tensor  $^4C^f$  can be expressed as:

$$\mathbf{C}^{f} = \frac{E_{f}}{(1+v_{f})(1-2v_{f})} \begin{pmatrix} 1-v_{f} & v_{f} & v_{f} & 0 & 0 & 0\\ v_{f} & 1-v_{f} & v_{f} & 0 & 0 & 0\\ v_{f} & v_{f} & 1-v_{f} & 0 & 0 & 0\\ 0 & 0 & 0 & \frac{1-2v_{f}}{2} & 0 & 0\\ 0 & 0 & 0 & 0 & \frac{1-2v_{f}}{2} & 0\\ 0 & 0 & 0 & 0 & 0 & \frac{1-2v_{f}}{2} \end{pmatrix}$$

$$(2)$$

where  $E_f$  and  $\nu_f$  are Young's modulus and Poisson's ratio of the fibers material.

Other important parameters in characterizing the fibrous network's mechanical behavior are its volume fraction and porosity. Volume fraction  $\phi$  represents the proportion of the total volume occupied by the fibers in the network and can be calculated as

$$\phi = \frac{V_f}{V_*},\tag{3}$$

where  $V_f$  is the fibers' volume and  $V_t$ , is the total volume of the RVE. The porosity  $\eta$  is defined as:

$$\eta = 1 - \phi = 1 - \frac{V_f}{V_t} = \frac{V_v}{V_t},\tag{4}$$

where  $V_v$  is the volume of voids in the specimen. These parameters affect key properties such as stiffness, strength, and overall deformation response.

# 2.2. Extracting effective property via homogenization

The asymptotic homogenization method, proposed by Bahvalov (Bahvalov, 1974) and further developed by Bensoussan, Lions, and

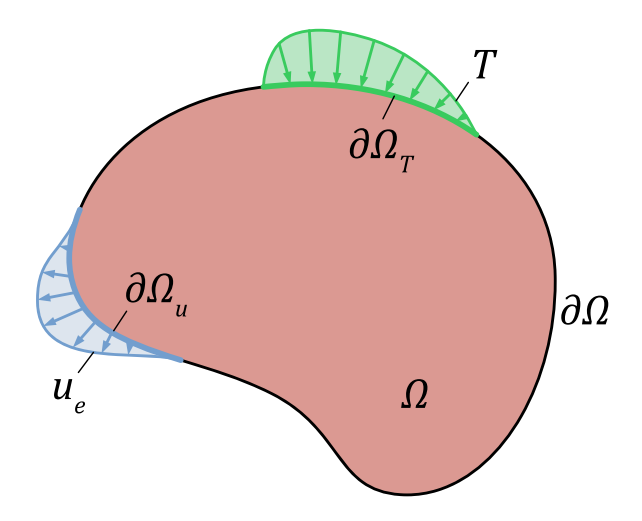


Fig. 2. Linear elasticity problem domain with boundary and applied boundary conditions.

Papanicolaou (Bensoussan et al., 1978), Sánchez-Palencia (Sánchez-Palencia, 1980), Pobedrja (Pobedrya, 1983), Bahvalov-Panasenko (Bahvalov and Panasenko, 1989), and others, is used to determine the effective properties of fibrous nonwoven materials among many other materials (Kouznetsova et al., 2004; Vazic et al., 2023, 2022b; He et al., 2020; Vazic et al., 2022a). The details of this method are well described in the works of Panasenko (Panasenko, 2008) and Sokolov (Ivanovich and Sokolov, 2010).

The main idea of asymptotic homogenization is to divide the solution domain into two distinct levels: the microscopic scale with a characteristic size of l and the macroscopic scale with a characteristic size of L, such that  $l \ll L$ . At the microscopic scale, the domain is represented as a heterogeneous structure with periodicity. At the macroscopic scale, the material is considered homogeneous with certain averaged characteristics.

As shown in Fig. 2, the governing equations for the linear elasticity within a domain  $\Omega$  with boundary  $\partial\Omega$  will take the form:

$$\varepsilon = \frac{1}{2} \left( \nabla \mathbf{u} + (\nabla \mathbf{u})^T \right) \tag{5}$$

$$\sigma = {}^{4}\mathbf{C} : \varepsilon \tag{6}$$

$$\nabla \cdot \mathbf{\sigma} = 0 \tag{7}$$

where u is displacements vector,  $\epsilon$  and  $\sigma$  denote strain and stress tensors respectively, and  $^4C$  denotes 4th rank tensor of elastic properties. The boundary conditions are presented as known displacements and surface tractions on the outer boundary:

$$\begin{cases} \mathbf{\sigma} \cdot \mathbf{n} = \mathbf{T}, & \mathbf{x} \in \partial \Omega_T \end{cases}$$
(8)

$$\mathbf{u} = \mathbf{u}_{o}, \qquad \mathbf{x} \in \partial \Omega_{u} \tag{9}$$

For the homogenization procedure, we will use the Voigt notation, according to which the stress and strain tensors are represented as a vector:

vector:
$$\boldsymbol{\varepsilon}^{v} = \begin{cases}
\varepsilon_{11} \\
\varepsilon_{22} \\
\varepsilon_{33} \\
2\varepsilon_{23} \\
2\varepsilon_{13} \\
2\varepsilon_{12}
\end{cases} = \begin{cases}
\varepsilon_{x} \\
\varepsilon_{y} \\
\varepsilon_{z} \\
\gamma_{yz} \\
\gamma_{xz} \\
\gamma_{xy}
\end{cases};$$

$$\boldsymbol{\sigma}^{v} = \begin{cases}
\sigma_{11} \\
\sigma_{22} \\
\sigma_{33} \\
\sigma_{23} \\
\sigma_{13} \\
\sigma_{13}
\end{cases} = \begin{cases}
\sigma_{x} \\
\sigma_{y} \\
\sigma_{z} \\
\tau_{yz} \\
\tau_{xz} \\
\tau_{xy}
\end{cases};$$
(10)

Then the stiffness can be determined as:

$$\langle \mathbf{\sigma}^{v} \rangle = \mathbf{C}^{v}_{eff} \langle \varepsilon^{v} \rangle, \tag{11}$$

where  $\mathbf{C}^{v}_{eff}$  is averaged matrix of elastic properties,  $\langle \boldsymbol{\epsilon}^{v} \rangle$  and  $\langle \boldsymbol{\sigma}^{v} \rangle$  are average strain and stress vectors within the volume of the RVE V, and are determined according to:

$$\langle \mathbf{\sigma}^{v} \rangle = \frac{1}{V} \int_{\Omega} \mathbf{\sigma}^{v}(\mathbf{x}) d\mathbf{x}, \tag{12}$$

$$\langle \mathbf{\varepsilon}^{v} \rangle = \frac{1}{V} \int_{O} \mathbf{\varepsilon}^{v}(\mathbf{x}) d\mathbf{x}.$$
 (13)

After the averaging process, any solutions of the system of Eqs. (5)–(7) with different boundary conditions (8)–(9) must satisfy Eq. (11). Therefore, to determine the matrix  $\mathbf{C}^v_{eff}$ , we need to solve 6 different boundary value problems, whose averaged parameters can be expressed as an equation:

$$\begin{bmatrix} \langle \mathbf{\sigma}_{1}^{v} \rangle & \langle \mathbf{\sigma}_{2}^{v} \rangle & \langle \mathbf{\sigma}_{3}^{v} \rangle & \langle \mathbf{\sigma}_{4}^{v} \rangle & \langle \mathbf{\sigma}_{5}^{v} \rangle & \langle \mathbf{\sigma}_{6}^{v} \rangle \end{bmatrix} \\
= \mathbf{C}_{eff}^{v} \begin{bmatrix} \langle \mathbf{\epsilon}_{1}^{v} \rangle & \langle \mathbf{\epsilon}_{2}^{v} \rangle & \langle \mathbf{\epsilon}_{2}^{v} \rangle & \langle \mathbf{\epsilon}_{4}^{v} \rangle & \langle \mathbf{\epsilon}_{5}^{v} \rangle & \langle \mathbf{\epsilon}_{6}^{v} \rangle \end{bmatrix} \tag{14}$$

Ωt

$$\Sigma = \mathbf{C}_{eff}^{v} \mathbf{E}. \tag{15}$$

And then by solving this equation for  $C_{eff}^v$ , we obtain

$$\mathbf{C}_{eff}^{v} = \mathbf{\Sigma} \mathbf{E}^{-1} \tag{16}$$

Here in (15) and (16) we employ matrix multiplication on the tensors written as matrices using Voigt notation, which yields a matrix as the result.

Fig. 3 shows three types of boundary conditions that are commonly used in the homogenization procedure of heterogeneous media. Here is a brief explanation of each:

- Kinematic Uniform Boundary Conditions (KUBC) (Hill, 1963; Bensoussan et al., 1978; Huet, 1990) assumes that the strain field is uniform on the boundary of a cell of a composite material (CM). This type of boundary condition is often used to determine the effective elastic properties of composites.
- Static Uniform Boundary Conditions (SUBC) (Hill, 1963; Bensoussan et al., 1978; Huet, 1990) assumes that the stress field is uniform on the boundary of a cell of a composite material. This type of boundary condition is often used to determine the effective strength properties of composites.
- Periodic Boundary Conditions (PBC) (Hashin and Shtrikman, 1963; Bahvalov and Panasenko, 1989; Panasenko, 2008; Ostoja-Starzewski, 2006) assumes that the stress and displacement fields are periodic within the domain, with periodicity corresponding to the cell size. This type of boundary condition is commonly employed to evaluate not only mechanical properties but also thermal and hygro properties. It also shows faster convergence of the field of interest, such as displacement or temperature fields.

Other types of BCs used for CM property identification include:

- Mixed uniform BCs (Moulinec and Suquet, 1994; Pahr and Böhm, 2008): These boundary conditions combine two or more types of boundary conditions to model more complex loading and deformation scenarios.
- Non-uniform boundary conditions (Geers et al., 2001): These boundary conditions assume that the external load or displacement is non-uniform across the unit cell of the composite material.

Although PBC captures the periodicity of the microstructure and it can lead to accurate homogenized properties, it requires a conjoint mesh on the opposite boundaries of the RVE, which can be challenging to achieve for random fibrous networks. KUBC, on the other hand, is simpler to implement and can be applied to any arbitrary geometry without the need for uniformity or periodicity, especially for random media. It is also computationally efficient, since it does not change

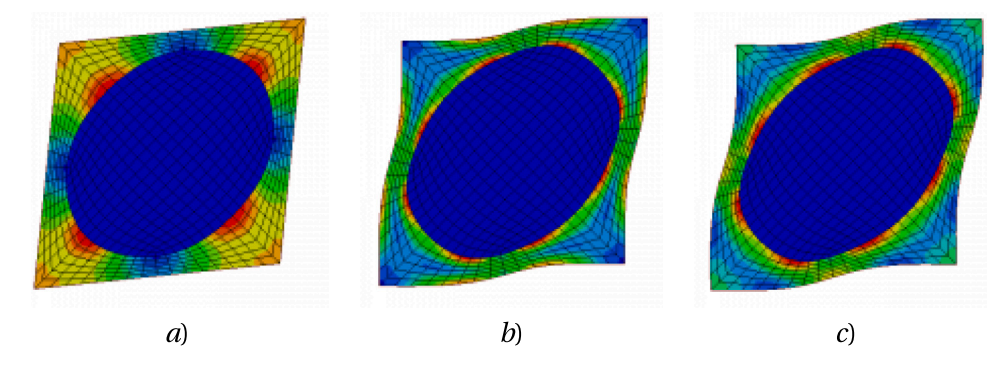


Fig. 3. Different types of boundary condition: kinematic uniform (a), static uniform (b) and periodic (c) boundary conditions.

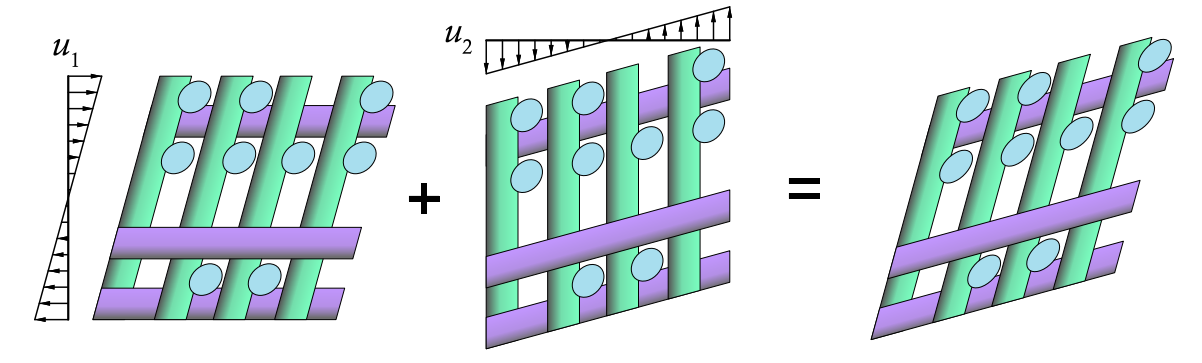


Fig. 4. Example of applying KUBC for shear loading.

the dimension of the resolving SLE, and can be applied to large-scale problems (Walters et al., 2021). Moreover, since one of the aims of this work was to build a numerical framework that is applicable to various types of networks, the KUBC approach was used in this study.

For KUBC two types of boundary conditions can be considered: the uniaxial tension along the ith direction and shear in i-j plane. For the first type of boundary condition, the boundary nodes' displacement will be calculated as:

$$\begin{cases} u_i = \frac{x_i}{L_i} \\ u_k = 0, & \text{for } k \neq i., \end{cases}$$
 (17)

where  $L_i$  is the RVE size along the *i*th direction. For the second type of boundary condition the boundary nodes' displacement will be:

$$\begin{cases} u_i = \frac{x_j}{2L_j} \\ u_j = \frac{x_i}{2L_i} \\ u_k = 0, \quad \text{for } k \neq i, j \end{cases}$$
 (18)

An example of boundary conditions for applying the shear loading is shown in Fig. 4.

Finally, the macroscopic strain tensor can be obtained by averaging the local strain tensor over the RVE through the following equations:

$$\mathbf{E} = \mathbf{I},$$

$$\mathbf{C}_{eff}^{v} = \mathbf{\Sigma}$$
(19)

#### 2.3. Computational workflow using fenicsx

For the numerical implementation, we chose FEniCSx framework (Scroggs et al., 2022b,a), a powerful and versatile, open-source computational tool. FEniCSx provides significant advancements over the legacy version of FEniCS, making it an ideal choice for developing an efficient and robust approach to homogenizing mechanical properties in our study. One primary motivation for selecting FEniCSx is its

open-source nature, which promotes inclusivity and accessibility to researchers regardless of their financial resources. This commitment to open science ensures that a broader community of researchers can leverage and benefit from the capabilities offered by FEniCSx. Moreover, FEniCSx offers a wide range of improvements and enhancements compared to its legacy version. It provides comprehensive support for various cell types and elements, along with features like memory parallelization and complex number support. These enhancements improve computational efficiency and extend the range of problems that can be effectively solved. Furthermore, FEniCSx incorporates an enhanced library design, contributing to the overall effectiveness and reliability of the framework in performing complex numerical simulations.

To ensure transparency and reproducibility, we have made all the code utilized in this study available on GitHub (Kuts and Walker, 2023). Sharing the codebase enables other researchers to easily access and verify the computational workflow, facilitating replicating our results and fostering further advancements in the field.

The generalized flowchart of the computational workflow is shown in Fig. 5. This framework comprises three main stages: preprocessing, solving, and postprocessing. The preprocessing stage involves mesh generation using GMSH (Geuzaine and Remacle, 2009), an open-source mesh generator. GMSH supports the generation of various mesh types, including structured, unstructured, and adaptive meshes, providing flexibility in mesh design. A notable feature of GMSH is its integration with the OpenCASCADE kernel, enabling the creation of complex 2D and 3D geometries using boundary representation (B-Rep) and constructive solid geometry (CSG) techniques. This capability is particularly valuable when simulating the mechanical properties of complex fibrous networks, as it allows for accurate geometry representation.

Additionally, GMSH provides multiple programming interfaces, including its own scripting language, C++, Python, and Julia. The availability of Python programming interfaces is advantageous since FEniCSx also utilizes Python as its primary programming language. This

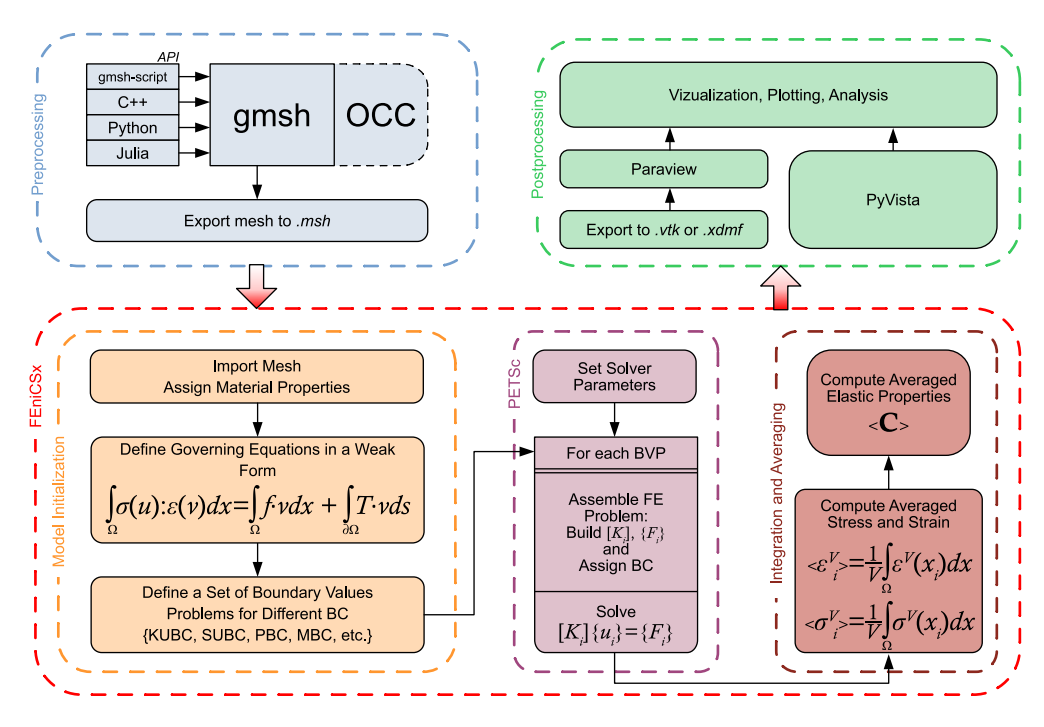


Fig. 5. Generalized workflow describing first-order homogenization using FEniCSx.

compatibility enables seamless integration between the mesh generation process in GMSH and the subsequent computation stage in FEniCSx. Furthermore, the option to use C++ or Julia programming interfaces offers the possibility to improve the performance and accelerate the computational speed, if required.

The main part of the computational workflow consists of three subparts: model initialization, solving the constitutive system of linear equations using PETSc (Balay et al., 1997, 2023), and computation of the averaged mechanical properties. For model initialization, the dolfinx.io module is employed, facilitating the import of the geometry generated in GMSH. Once the geometry is imported, we define the governing equations described by Eq. (5)–(7) in weak form using the Unified Form Language (UFL) (Alnæs et al., 2014). The weak form of these equations takes the following form:

$$a(\mathbf{u}, \mathbf{v}) = L(\mathbf{v}), \qquad \forall \mathbf{v} \in \hat{V}^3$$
 (20)

where **v** is a test function, defined on the test functions space  $\hat{V}^3$ , **u** is the trial function which represents an unknown displacements to be solved,  $a(\cdot,\cdot)$  and  $L(\cdot)$  are bilinear and linear form, respectively, which are calculated as:

$$a(\mathbf{u}, \mathbf{v}) = \int_{\Omega} \mathbf{\sigma}(\mathbf{u}) : \mathbf{\varepsilon}(\mathbf{v}) d\mathbf{x}$$
 (21)

$$L(\mathbf{v}) = \int_{\Omega} \mathbf{f} \cdot \mathbf{v} d\mathbf{x} + \int_{\partial \Omega_T} \mathbf{T} \cdot \mathbf{v} d\mathbf{x}$$
 (22)

The bilinear form  $a(\mathbf{u}, \mathbf{v})$  and the linear form  $L(\mathbf{v})$  further are used to assemble stiffness matrix  $\mathbf{K}$  and forces vector  $\mathbf{f}$  which govern a constitutive system of linear equations:

$$\mathbf{K}\mathbf{u}^n = \mathbf{f} \tag{23}$$

where  $\mathbf{u}^n \in \mathbb{R}^{3N}$  is a vector of nodal displacements with N - number of degrees of freedom. The solution of the system (23) is obtained using PETSc, which provides various Krylov subspace methods for solving large-scale linear systems efficiently.

The computation of averaged mechanical properties involves the calculation of integrals in Eqs. (12) and (13). FEniCSx simplifies this procedure by utilizing the dolfinx.fem.assemble function, which allows to compute integrals of specified forms formulated using UFL. The

final calculation of the averaged mechanical properties can be achieved through Eq. (16).

Lastly, in the postprocessing stage, both ParaView (Ahrens et al., 2005; Ayachit, 2015) and PyVista (Sullivan and Kaszynski, 2019) were used for the visualization of the computed results. ParaView, a widely recognized and extensively used scientific visualization software, provided us with a comprehensive set of tools for analyzing and visualizing simulation data. To facilitate the visualization process, the mesh with calculated fields is exported to the VTK or XDMF file formats directly, which seamlessly integrates with ParaView. Leveraging ParaView enables interactive exploration and in-depth visualization of the data. Additionally, we utilized PyVista, a Python library, for direct visualization within the Jupyter Notebook environment. PyVista offered a convenient interface for generating high-quality visualizations directly from our computational workflow. With PyVista, we visualized the mesh, displayed the computed results, and created interactive plots within the familiar Jupyter Notebook interface.

# 3. Model setup

This section highlights the numerical model from geometry generation to numerical analysis. It should be noted that in this study, we employed the "quasi-BCC nanogrid" microstructure as previously introduced in Cheng et al. (2023). The choice of this microstructure was motivated by its simplicity and inherent randomness, which make it ideal for showcasing the concept of our numerical approach.

#### 3.1. Geometry creation of the fibrous porous network

The geometry of the investigated material can be described as a quasi-structured fibrous medium with an orthogonal fiber arrangement. The lattice is composed of a triad of three mutually orthogonal fibers with a circular cross-section (see Fig. 6–I), intersecting by an amount of  $s_i = d_f \gamma$ , where  $d_f$  is the fiber diameter, and  $\gamma$  is the intersection ratio. Each fiber axis is then shifted from the triad center by  $s_{\rm off} = 0.5(d_f - s_i)$ .

Within the RVE, the fiber triads are located at the nodes of a simple cubic lattice with a pitch  $P_l$ . The maximum number of fibers along one axis is  $N^2$ , where N is a grid size. However, structural defects in the form of vacancies (absence of fibers) may occur, resulting in the actual

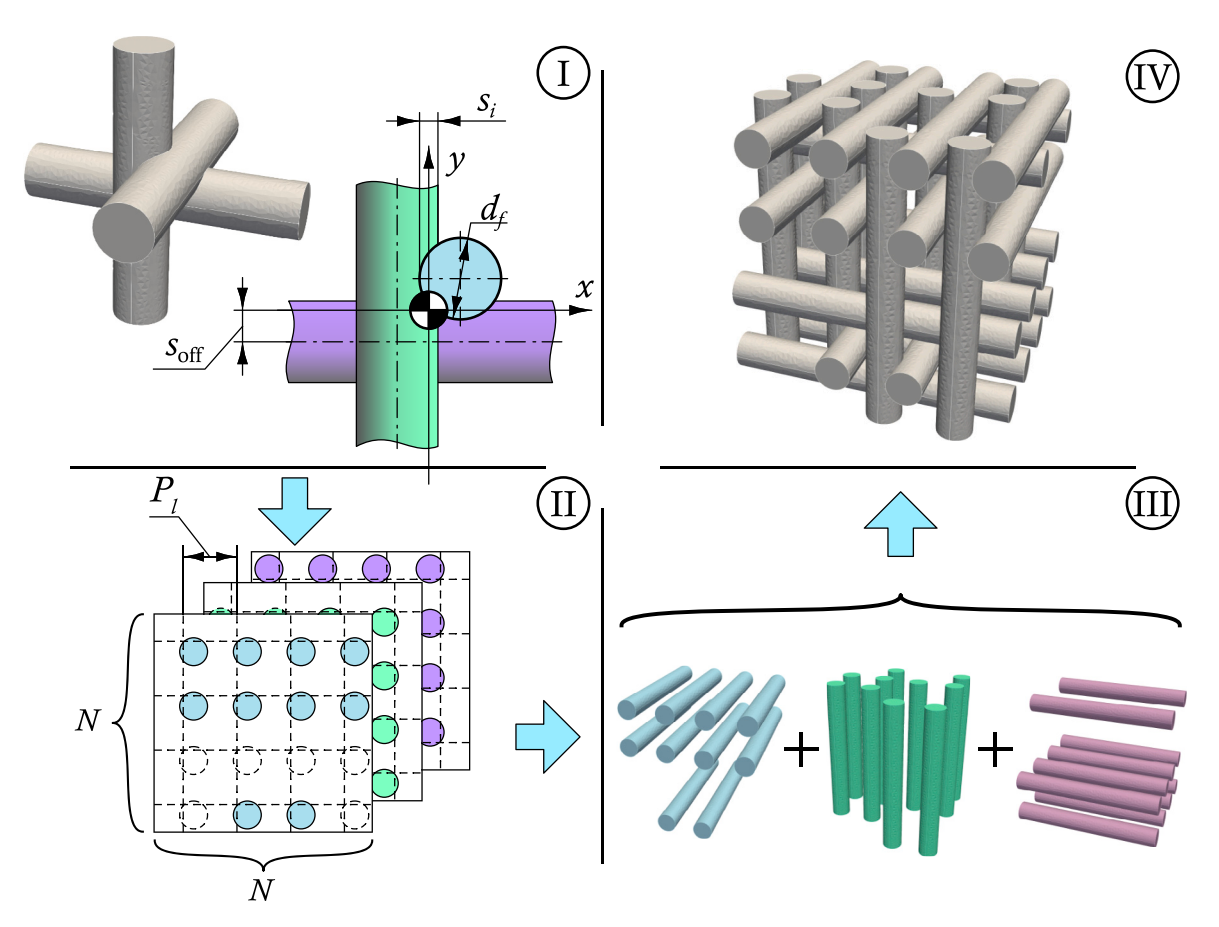


Fig. 6. Structure and geometry of fibrous network: I — geometry of a single fibers' triad with diameter  $d_f$  and intersection  $s_i$ ; II — generation of fibers within a grid  $N \times N$  with a pitch  $P_i$  along each basis axes for a given fillness parameter  $\psi$ ; III — fusion of all three sets of fibers; IV — result network.

number of fibers along each axis varying within the range  $1 \le m \le N^2$ . The fiber fill fraction of the structure is characterized by the parameter "fillness"  $\psi = \frac{m}{N^2}$ . If the number of fibers is different in each direction, the structure will be characterized by three respective coefficients ( $\psi_x$ ,  $\psi_y$ ,  $\psi_z$ ):

$$\psi_i = \frac{m_i}{N^2}. (24)$$

However, in the current work, the network with equal fillness along all axis  $(\psi_x = \psi_y = \psi_z = \psi)$  is considered. Thus, the overall actual number of fibers within the RVE is  $N_f = 3m$ .

To ensure the connectivity of the structure during RVE generation, the vacancies are randomly distributed on two of the base planes (see Fig. 6–II), followed by the computation of all fiber intersections along these two directions. Fibers along the third direction are generated at existing nodes without repetition and then supplemented randomly to reach the desired quantity. Subsequently, cylindrical fibers are generated at the obtained nodes (see Fig. 6–III) and fused together into a single body using the fusion (i.e., merge) operation (Fig. 6–IV).

It is worth noting that in this work, it is assumed that fibers can only intersect from one side by a fixed amount. Thus, the maximum diameter for the chosen pitch is related by the following dependence:

$$D_f < \frac{P_l}{2 - \gamma}.\tag{25}$$

#### 3.2. Problem description

This study focuses on a chemically bonded quasi-structured fibrous media composed of PP fibers. The main properties of the typical PP fibers are presented in Table 1. The network structure is designed

**Table 1**The main properties of the typical PP fibers.

r . r	- J F	
Property	Unit	Value
Young's modulus	GPa	1.8
Poisson's ratio	-	0.43
Elongation, Yield	_	0.10-0.12
Elongation, Break	_	0.50-1.45
Density	<u>g</u> mL	0.905

to resemble a configuration described in the literature (Cheng et al., 2023). It is assumed that all fibers intersect with each other, and through a bonding process, the entire network forms a cohesive solid body.

Primarily, the effect of RVE size was investigated through two types of networks: (i) a structured mesh and (ii) a quasi-structured mesh with fillness ratio  $\psi=0.5$ . The results of the first investigation were used to define the size of the RVE for the second investigation.

For the structured grid convergence analysis, a porosity of 0.5 was chosen, with a fiber diameter of 0.2 mm and an intersection ratio of 25%. To achieve the target porosity, the spacing between fibers was set at 0.423 mm. Several meshes were generated with varying parameters, including the number of fibers per axis, the overall number of fibers within the RVE, and mesh parameters such as the overall number of nodes and elements. The specific values for these parameters are listed in Table 2. Additionally, Fig. 7(a-b) illustrates the RVEs of structured networks with scale ratios of 1, 4, and 7.

Similarly, the investigation of convergence on the quasi-structured network was performed. The geometrical fiber parameters such as their diameter and the intersection ratio remained consistent with the

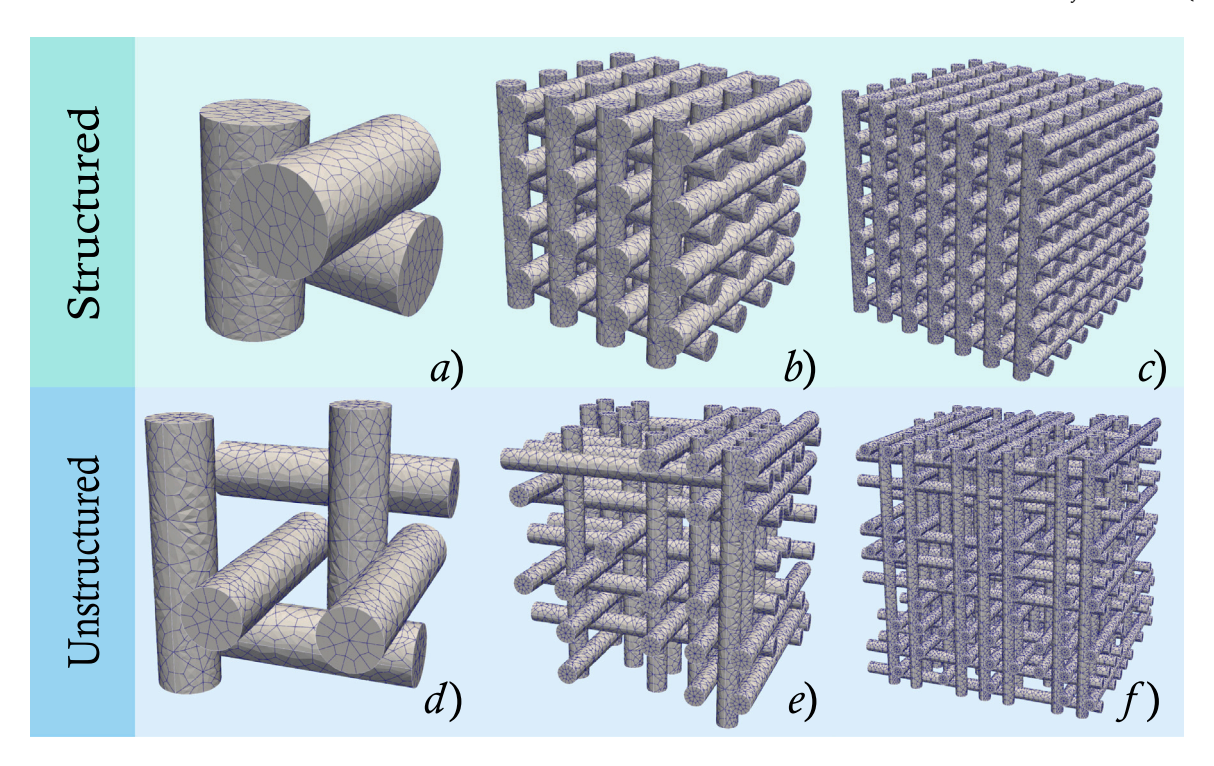


Fig. 7. Examples of the mesh used for the study of the RVE size on the structured (a-c) and unstructured (d-f) networks with different scale ratios: a) scale ratio = 1, b) scale ratio = 4, c) scale ratio = 7, d) scale ratio = 2, e) scale ratio = 6, f) scale ratio = 10.

Table 2
Parameters of the RVE of structured network.

Network type	Scale ratio	Number of fibers	Number of DoFs	Number of elements
	1	3	20,778	3,636
	2	12	79,820	14,260
	3	27	189,452	34,508
Structured	4	48	427,372	77,648
	5	75	835,624	150,362
	6	108	1,353,934	244,362
	7	147	2,085,690	376,530
	2	6	37,866	6,782
	4	24	161,224	30,047
Unstructured	6	54	498,865	92,481
	8	96	1,080,284	200,570
	10	150	2,072,314	383,332

structured network, while the porosity was increased to 0.744. The generated networks for scale ratios of 2, 6, and 8 are depicted in Fig. 7(d-f).

The second and primary investigations are dedicated to studying the influence of porosity and fiber geometry on the effective mechanical properties of the fibrous porous network. The selected network structure enables the examination of the mechanical properties of the medium with specific porosity values and varying diameters of fibers. This is achieved by adjusting the density of the fiber grid. Additionally, the impact of intersection magnitude, which affects the bonding process, is examined to understand its effect on the mechanical properties. The grid size N of the network was selected as 6 based on the findings from investigating the size effect of the RVE. The grid pitch  $P_l$  was 50  $\mu$ m, so the length of the RVE was  $L = P_l N = 300~\mu$ m. The variable parameters of the investigated network are shown in Table 3.

#### 3.3. Numerical setup

The numerical setup employed in this study encompassed an unstructured FEM-mesh comprising 27 nodal second-order hexahedral elements. This choice of mesh allowed for an accurate representation of the geometric features and facilitated efficient computations within the FEniCSx framework. The mesh sizes of the RVEs used in this investigation varied within a range of  $\approx 0.4 \times 10^6$  DoFs up to  $\approx 1.8 \times 10^6$  DoFs. Additionally, a convergence study was performed using meshes of up to  $\approx 2.2 \times 10^6$  DoFs.

For solving the governing system (23), we utilized the conjugate gradient (CG) method, combined with the multigrid preconditioner. This combination of solvers and preconditioners ensured rapid convergence and efficient solutions to the problem at hand.

In our specific project, the utilization of the multigrid preconditioner and conjugate gradient (CG) solver proved to be effective in efficiently handling fairly large problems. For instance, a problem consisting of approximately  $4\times10^5$  DoFs was solved within a computational time of fewer than 10 min. These computations were performed on a personal computer equipped with an i7-1165G7 2.8 GHz processor and 16 GB of RAM. Specifically, the entire computational process was executed within a Docker container installed on Windows Subsystem for Linux 2 (WSL2). It should be noted that running the computations on a native Linux system results in additional performance improvements.

# 3.4. Mesh convergence

We investigated the dependence of solution accuracy on element size through systematic variations in mesh parameters and observation of convergence behavior. The convergence study was performed on a representative cell containing a single triad of fibers, with the depicted meshes shown in Fig. 8.

We evaluated the accuracy of the numerical solution by evaluating the  $L_2$  norm of the error for the components of the elasticity tensor  $\mathbf{C}_{eff}^h$  compared to the reference solution  $\tilde{\mathbf{C}}_{eff}$  (see. Fig. 8-a). The  $L_2$  norm is defined as follow:

$$L_2(\mathbf{A}) = \max_i \lambda_i, \tag{26}$$

**Table 3**Geometrical properties of the investigated RVEs.

Fibers number	Fillness	Fibers' diameter	Porosity	Intersection ratio	Fibers number	Fillness	Fibers' diameter	Porosity	Intersection ratio
$N_f$	Ψ	$d_f$	φ	γ	$N_f$	Ψ	$d_f$	φ	γ
-	-	$mm \times 10^{-2}$	-	-	-	_	$mm \times 10^{-2}$	-	-
12	0.33	1.800	0.9	0.25	24	0.67	1.290	0.9	0.40
18	0.50	1.470	0.9	0.25	30	0.83	1.155	0.9	0.40
24	0.67	1.275	0.9	0.25	12	0.33	2.590	0.8	0.40
30	0.83	1.140	0.9	0.25	18	0.50	2.120	0.8	0.40
12	0.33	2.550	0.8	0.25	24	0.67	1.845	0.8	0.40
18	0.50	2.085	0.8	0.25	30	0.83	1.655	0.8	0.40
24	0.67	1.810	0.8	0.25	36	1.00	1.515	0.8	0.40
30	0.83	1.620	0.8	0.25	18	0.50	2.620	0.7	0.40
36	1.00	1.480	0.8	0.25	24	0.67	2.278	0.7	0.40
18	0.50	2.560	0.7	0.25	30	0.83	2.045	0.7	0.40
24	0.67	2.221	0.7	0.25	36	1.00	1.875	0.7	0.40
30	0.83	1.990	0.7	0.25	18	0.50	3.040	0.6	0.40
36	1.00	1.820	0.7	0.25	24	0.67	2.645	0.6	0.40
12	0.33	1.815	0.9	0.40	30	0.83	2.378	0.6	0.40
18	0.50	1.485	0.9	0.40	36	1.00	2.183	0.6	0.40

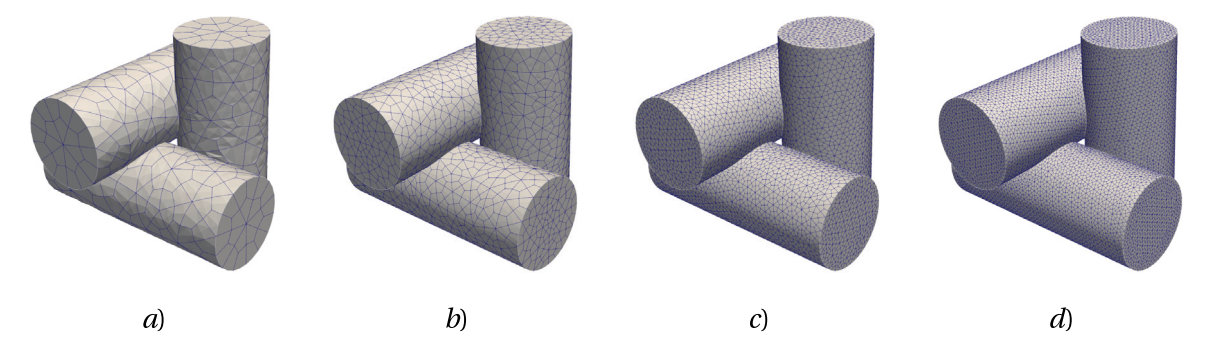


Fig. 8. Meshes used for mesh convergence tests: coarse mesh with  $h=4.7~\mu m$  (a), mean mesh with  $h=2.6~\mu m$  (b), fine mesh with  $h=1.5~\mu m$  (c) and reference mesh with  $h=1.0~\mu m$  (d).

**Table 4** Parameters of the RVE used for mesh convergence investigation.

Element size, µm	DoFs	Elements	$\frac{L_2(\mathbf{C}_{eff}^h - \mathbf{\tilde{C}}_{eff})}{L_2(\mathbf{\tilde{C}}_{eff})}$
4.7	11,194	2,052	$38.5 \times 10^{-3}$
2.6	67,206	10,702	$7.69 \times 10^{-3}$
1.5	384,562	55,270	$1.57 \times 10^{-3}$
1.0	999,194	137,736	-

where  $\lambda_i$  is an ith eigenvalue of the tensor A. In our case it corresponds to the maximum eigenvalue  $\lambda_{max}^c$  of the elasticity tensor C. The reference solution  $\tilde{C}$  was obtained using a mesh with an element size of approximately 1  $\mu$  m. Model parameters and corresponding solution errors are provided in Table 4. Fig. 9 shows the relationship between the error and element size. Through regression analysis, we determined the convergence rate to be approximately  $O(h^{2.61})$ , where h represents the element size.

# 4. Simulation results and discussion

The following subsections provide an in-depth discussion of the results of our case studies.

#### 4.1. Anisotropy of mechanical properties

The structure of the selected fibrous media exhibits pronounced asymmetry even in the case of a fully structured case (fillness=1.0, see Fig. 7), leading to the emergence of complex stress states even under KUBC conditions.

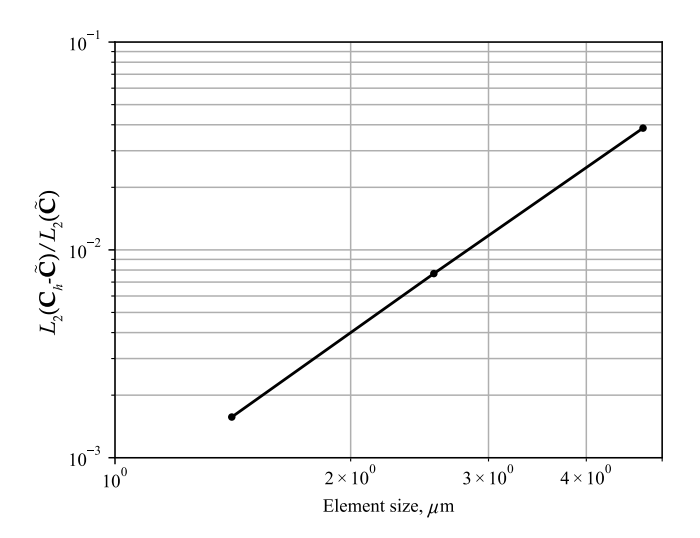


Fig. 9.  $L_2$  norm of relative error of effective matrix of elasticity for different average mesh size.

Due to the weak inter-fiber connectivity, individual fibers are subjected to bending under shear loading. For example, Fig. 10 illustrates the displacements fields for an RVE with porosity  $\phi=0.8$ , fiber diameter  $d_f=25.5~\mu\mathrm{m}$  and fillness  $\psi=0.333$  subjected to tensile loading (a) and shear loading (b), with a deformation scale of 0.5. All these factors contribute to the emergence of additional interdependencies between the shear and tensile components of the elasticity matrix. In the case

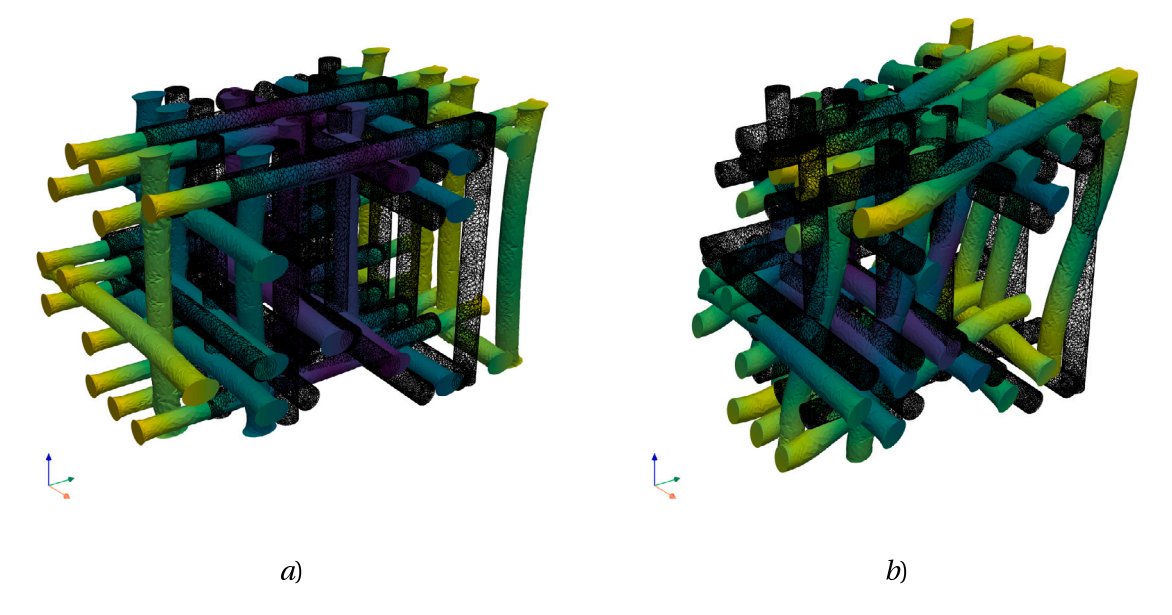


Fig. 10. Displacements fields for uniform tension (a) and shear(b) of RVE with porosity  $\phi = 0.8$ , fibers' diameter  $d_f = 25.5~\mu m$  and fillness  $\psi = 0.333$ .

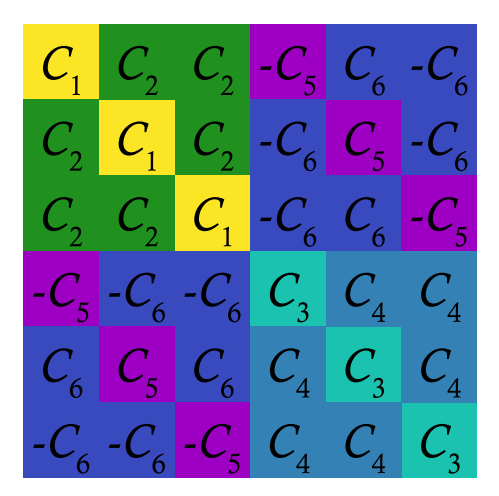


Fig. 11. Structure of the matrix of elastic properties.

where an equal number of fibers are present along each direction of the base lattice, the elasticity matrix will consist of six distinct components, as shown in Fig. 11. It should be mentioned that, due to randomness in structure and computational error, these six components have a variation in values. To represent these variations, min/max ranges are also shown in Figs. 12–14 in addition to the mean values. These components will be further discussed in the following subsections.

#### 4.2. Investigation of the scale effect

Previously, in works (Huet, 1990, 1999; Alzebdeh et al., 1998; Ostoja-Starzewski, 2006) was shown that for heterogeneous networks, an improperly chosen mesoscale window can lead to inappropriate results since the volume element is not further "representative". Thus, in work (Ostoja-Starzewski, 2006), the SVE was introduced, and it was demonstrated that as the mesoscale size increased, it tended to the RVE. In the following subsection, we examine the effect of the unit cell size to determine the appropriate size of the mesoscale window, which can be considered as representative (Kouznetsova, 2002).

The resulting values of the elasticity tensor components, namely  $C_1$ and  $C_4$ , for various sizes of the unit cell are illustrated in Fig. 12. The analysis was performed on both structured networks (with a fillness of  $\psi = 1.0$ ) and quasi-structured (heterogeneous) networks (with a fillness of  $\psi = 0.5$ ), constructed according to the parameters outlined in Table 2, respectively. In Fig. 12-a, which represents the component  $C_1$ , it is evident that the value of  $C_1$  decreases with the increase in the unit cell size, controlled by the base grid size N. The same dependency on unit cell size is observed for components  $C_2$  and  $C_3$  as well. However, the value of the  $C_4$  component increases with an increase in the unit cell size and these variations are relatively small for the quasi-structured networks. Additionally, it should be noticed that component  $C_1$  shows very small variations, whereas component  $C_4$  displays a noticeable variation, which increases with higher network fillness and decreases with larger unit cell size. It can be explained by the fact that the components of the elasticity tensor, which corresponded to the  $C_1$ , were responsible only for tension along the basis axes and depended only on the cross-section area, which was equal for each unit cell along all three basis axes. However, component  $C_4$  mainly depends on the fibers' connection, which is not constant due to the asymmetry of the connection within the triad (see Fig. 6) and the heterogeneous structure of unit cells with fillness  $\psi \neq 1$ . It is worth mentioning that the components  $C_5$  and  $C_6$  exhibit similar behavior as component  $C_4$ .

While it is commonly accepted that the KUBC overestimates the elastic parameters of the investigated material, Fig. 12 demonstrates an opposite trend for component  $C_4$ . Moreover, it is important to note that while the change in the unit cell size has a significant impact on the elastic properties of materials with a structured fiber, resulting in a 33% change in the value of component  $C_1$  and over 75% change in the value of component  $C_4$ , its effect on materials with heterogeneous fibers is much smaller. However, increasing the unit cell size considerably reduces the variability of components  $C_4$ ,  $C_5$ , and  $C_6$  for heterogeneous materials, whereas its effect on the variation of elastic properties in structured materials is negligible.

Furthermore, this investigation aids in determining the optimal unit cell size to balance computational efficiency and acceptable accuracy. Based on these considerations, a unit cell with a base grid size of N=6 was chosen for the subsequent investigation described in Section 4.3 and will be considered as the RVE.

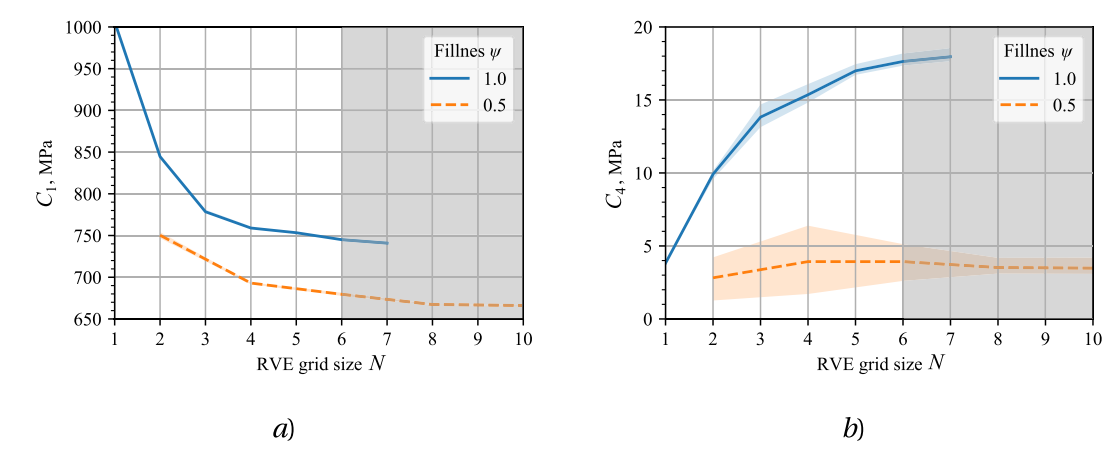


Fig. 12. The scale effect of unit cell on the components of the elasticity tensor: (a)  $C_1$  and (b)  $C_4$ .

#### 4.3. Influence of fibers diameter and porosity

Given the significant influence of fiber diameter on the mechanical properties, particularly the strength and stiffness, of fibrous porous materials, this section focuses on examining the response of the elasticity tensor with respect to variations in fiber diameter. Specifically, Fig. 13 illustrates the relationship between the components of the elasticity tensor and the diameter of the fibers for RVEs with an intersection ratio of  $\gamma=0.25$  for different values of porosity.

These plots demonstrate that as the porosity increases, the components of the elasticity tensor C decrease. A closer look also reveals that the largest change is observed for the porosity of  $\phi=0.7$ , while for the porosity of  $\phi=0.9$ , the changes are nearly negligible and comparable to computational errors. Additionally, as the porosity decreases, there is a noticeable reduction in the components of the elasticity tensor when the fiber diameter size increases. However, the most significant changes are observed in the absolute values of components  $C_1, C_3$ , and  $C_2$ . At a certain point (i.e., higher porosity), these components reach a stable value, and even a slight increase is observed as the role of fibers becomes minimal.

In contrast, components  $C_4$ ,  $C_5$ , and  $C_6$  do not reach a stable value. Furthermore, a 50% increase in fiber diameter leads to a multiple decrease in the values of these components. Another interesting observation is that increasing the fiber diameter leads to an increase in the variation of components  $C_4$ ,  $C_5$ , and  $C_6$ .

The maximum value is observed for components  $C_1$  and the minimal value — for  $C_4$ . Moreover, all components can be ordered as follows  $C_1 \gg C_3 > C_2 \gg C_6 > C_5 > C4$ . The low values of components  $C_4$ - $C_6$  is explained by the cubic structure of the network. In the limiting case with high randomness, it may come to the case of anisotropy with cubic symmetry, where these components are equal to zero, which can be observed from the trends of these components plots (see Fig. 13). As it was mentioned in Section 4.2, the component  $C_1$  is responsible for the tension along the basis axes. And since the fibers are also located along them, this component has the highest value. The component  $C_3$  is responsible for shear in basis planes, and its low value can be explained by the fact that fibers have weak connections, and during shear, they mainly exhibit bending deformations. Finally, a low value of the component  $C_2$  means that for the chosen geometry, compression along one of the basis axes has little effect on deformation along two other axes.

Similarly, the results for RVEs with an intersection ratio of  $\gamma=0.4$  are presented in Fig. 14. The same effects are observed in these cases as well. However, reaching a stable value is only observed for higher porosities of  $\phi=0.8$  and  $\phi=0.9$ . The changes in components  $C_1$ ,  $C_2$ , and  $C_3$  for a porosity of  $\phi=0.7$  are approximately 30 MPa, 15 MPa,

and 18 MPa, respectively. In relative terms, these changes correspond to approximately 4%, 20%, and 21%, respectively. For the porosity of  $\phi=0.6$ , the changes are approximately 60 MPa (7.3%), 30 MPa (30%), and 28 MPa (24%), respectively. Meanwhile, components  $C_4$ ,  $C_5$ , and  $C_6$  decrease by a factor of 2, 3, and 2.5, respectively.

Furthermore, it should be noted that the components of the elasticity tensor C for networks with an intersection ratio of  $\gamma=0.4$  are significantly larger compared to those with  $\gamma=0.25$ . For example, the increase in the  $C_1$  component is 3.1% for  $\phi=0.9$ , 5.2% for  $\phi=0.8$ , and 10% for  $\phi=0.7$ .

#### 5. Conclusion

The present study introduces a computational model based on the finite element method, which serves as a robust tool for simulating the mechanical properties of porous non-woven fibrous media. This model incorporates the geometric and material characteristics of the fibers and the void spaces, enabling a consistent analysis of the material's mechanical response. Through systematically varying parameters such as fiber size, porosity, and fiber intersection ratio, we explored their impacts on the mechanical properties of fibrous porous materials.

The results demonstrate that the material's porosity and fibers' intersection ratio are the primary factors influencing its mechanical behavior within the elastic region. A 10% increase in porosity results in a corresponding up to 10% increase in the value of the  $C_1$  component, assuming the diameter remains constant. Similarly, when the intersection ratio  $\gamma$  is increased from 0.25 to 0.4, there is a 7.3% increase in the value of the  $C_1$  component.

For the investigated structure it was observed that as the fiber diameter increases, the structural fillness of the material decreases, even at a fixed porosity. This leads to a higher level of randomness in the material's structure. Conversely, for smaller fiber diameters, the random fibrous network becomes more structured. This insight provides valuable knowledge for understanding and designing porous non-woven fibrous media, as the level of structural filling directly affects their mechanical properties. Furthermore, the study reveals that the impact of fiber diameter on the mechanical behavior of the material depends on the porosity. For materials with low porosity, both fiber diameter and fillness factor play significant roles in determining the material's properties. In contrast, materials with high porosity exhibit minimal sensitivity to changes in fiber diameter and fillness.

The analysis of the elasticity tensor components provides valuable insights into the mechanical behavior of the material. Specifically, increasing the fiber diameter leads to a reduction in these components, particularly for  $C_1$ ,  $C_2$ , and  $C_3$ . For example, doubling the fiber diameter results in a decrease of up to 60 MPa in  $C_1$  and 25

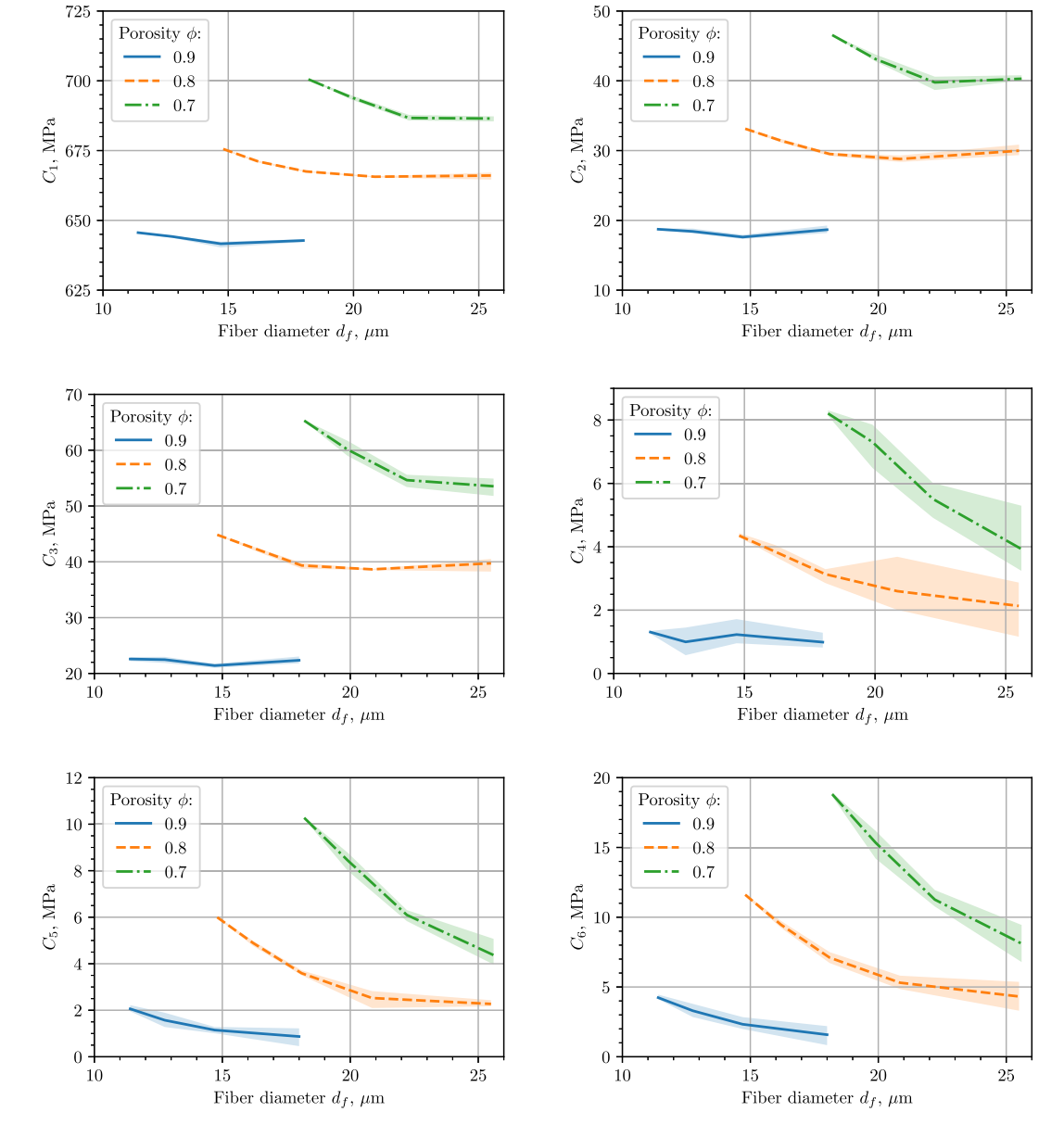


Fig. 13. Effect of fiber diameter on components of the tensor of elasticity for the network with  $\gamma = 0.25$ .

MPa in  $C_3$ . However, it is worth noting that these changes, while significant, are small in relative value, ranging from 7.3% for  $C_1$  to 24% for  $C_3$ . Moreover, the  $C_4$ ,  $C_5$ , and  $C_6$  components exhibit even more pronounced reductions, with  $C_4$  decreasing by more than twice and  $C_5$  and  $C_6$  exhibiting approximately three times reduction. This behavior can be attributed to the increase in the heterogeneity in the material's structure caused by larger fiber diameters, which subsequently leads to reduced anisotropy. These findings align with previous research (Bosco et al., 2017; Cucumazzo et al., 2021; Karakoc et al., 2020), further confirming the observed effect. Moreover, the study highlights the influence of fiber diameter and fillness factor on the variation of the elasticity tensor components. It was observed that increasing the fiber diameter and decreasing the fillness factor result in an increased variation of the  $C_4$ ,  $C_5$ , and  $C_6$  components, while the variation of the  $C_1$ ,  $C_2$ , and  $C_3$  components remains relatively unchanged.

At the same time, investigation of the RVE?s size effect on the material's behavior showed that increasing the size of the RVE leads to an increase in the number of fibers, reduces high variation in the  $C_4$ ,  $C_5$ , and  $C_6$  components. These findings provide valuable insights into the computational strategy for modeling non-woven fibrous media. While scaling up the RVE leads to a higher-dimensional system in the finite element method, thus stabilizing the averaged values, it may present computational challenges. Therefore, alternative approaches, such as two-scale modeling of the media, show promise in addressing these challenges. The two-scale modeling approach involves simulating various variations of the porous material at the microscale and not only calculating the equivalent values of the elastic properties but also their dispersion. Subsequently, at the mesoscale, the material is modeled as a continuum with spatial distributions of properties based on microscale-defined intrinsic laws. This approach shares similarities with the utilization of Stochastic Volume Elements (Mansour et al.,

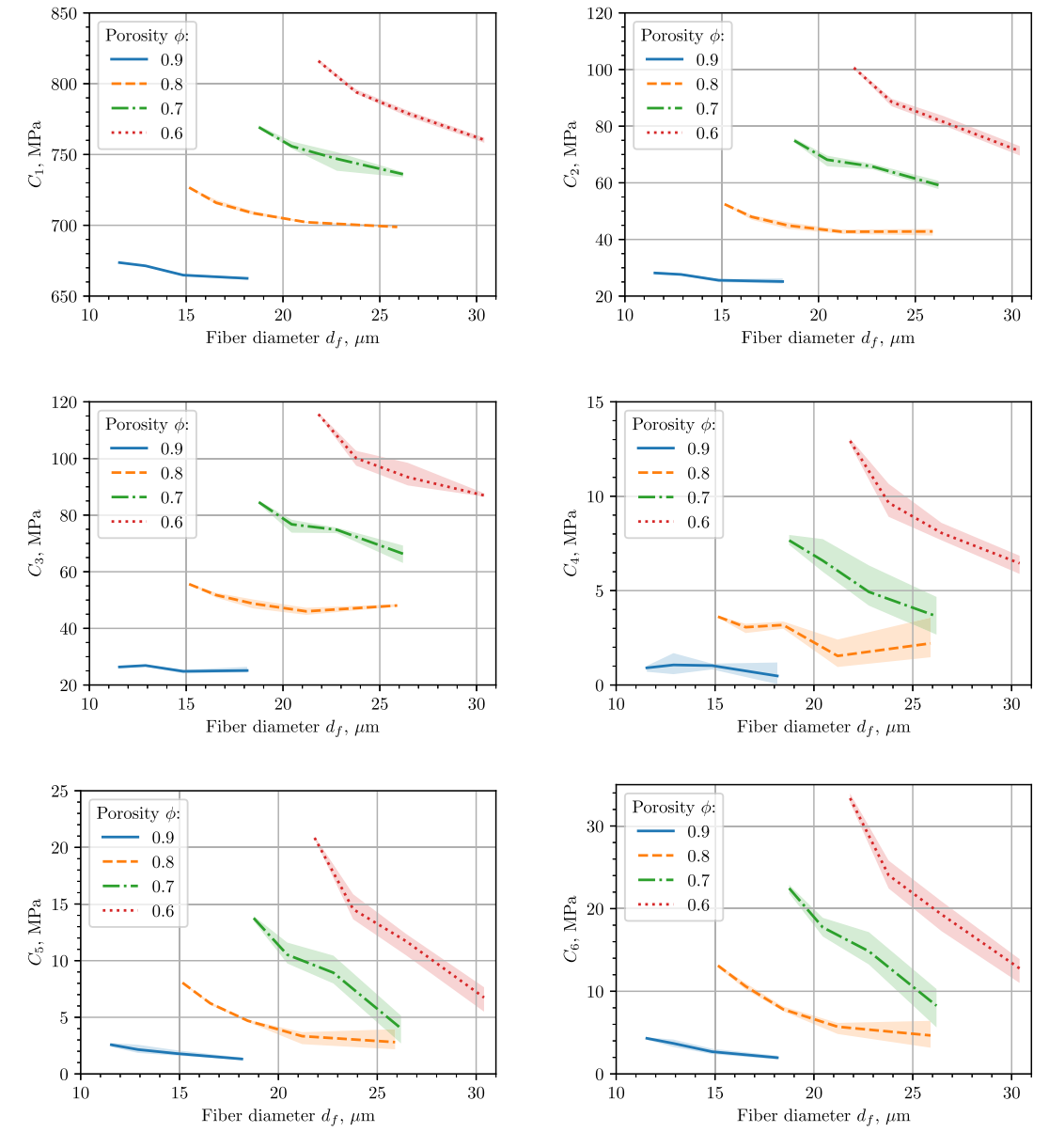


Fig. 14. Effect of fiber diameter on components of the tensor of elasticity for the network with  $\gamma = 0.4$ .

2019; Mansour and Kulachenko, 2022) or Stochastic Local FEM (Pivovarov et al., 2019, 2022). However, modeling the random properties requires the application of uncertainty quantification methods, which will be the focus of future work.

#### CRediT authorship contribution statement

**Mikhail Kuts:** Algorithms, Software, Modeling, Analysis, Writing – original draft & editing. **James Walker:** Software, Network geometry generation, Modeling. **Pania Newell:** Conceptualization, Supervision, Writing – review & editing, Funding acquisition.

#### Declaration of competing interest

The authors declare that they have no known competing financial interests or personal relationships that could have appeared to influence the work reported in this paper.

#### Data availability

Data will be made available on request.

# Declaration of Generative AI and AI-assisted technologies in the writing process

During the preparation of this work, the author(s) used ChatGPT to reduce grammar errors and enhance readability of the original draft of this manuscript. After utilizing this tool, the author(s) reviewed and edited the content as necessary, and take(s) full responsibility for the content of the publication.

#### Acknowledgments

This work was supported by the National Science Foundation, United States under award No 2033979 through the division of Civil, Mechanical, and Manufacturing Innovation (CMMI).

### References

Ahrens, James, Geveci, Berk, Law, Charles, 2005. In: Hansen, Charlesa D., Johnson, Christophera R. (Eds.), Visualization Handbook. In: Chap. ParaView: An End-User Tool for Large Data Visualization, Elsevier Inc., Burlington, MA, USA, pp. 717–731.

- Alnæs, Martina S., Logg, Anders, Ølgaard, Kristiana B., Rognes, Mariea E., Wells, Gartha N., 2014. Unified form language: A domain-specific language for weak formulations of partial differential equations. ACM Trans. Math. Software 40 (2).
- Alzebdeh, K., Jasiuk, I., Ostoja-Starzewski, M., 1998. Scale and boundary conditions effects in elasticity and damage mechanics of random composites. pp. 65–80.
- Ayachit, Utkarsh, 2015. The Paraview Guide a Parallel Visualization Application. Kitware. Inc..
- Bahvalov, N., 1974. Averaged characteristics of bodies with periodic structure. Dokl. Akad. Nauk SSSR 218, 1046–1048.
- Bahvalov, N., Panasenko, G., 1989. Homogenisation: Averaging Processes in Periodic Media, vol. 36. Springer Netherlands.
- Balay, Satish, Abhyankar, Shrirang, Adams, Marka F., Benson, Steven, Brown, Jed, Brune, Peter, Buschelman, Kris, Constantinescu, Emila M., Dalcin, Lisandro, Dener, Alp, Eijkhout, Victor, Faibussowitsch, Jacob, Gropp, Williama D., Hapla, Vá, Isaac, Tobin, Jolivet, Pierre, Karpeev, Dmitry, Kaushik, Dinesh, Knepley, Matthewa G., Kong, Fande, Kruger, Scott, May, Davea A., McInnes, Loisa Curfman, Mills, Richarda Tran, Mitchell, Lawrence, Munson, Todd, Roman, Josea E., Rupp, Karl, Sanan, Patrick, Sarich, Jason, Smith, Barrya F., Zampini, Stefano, Zhang, Hong, Zhang, Hong, Zhang, Junchao, 2023. PETSc web page. https://petsc.org/.
- Balay, Satish, Gropp, Williama D., McInnes, Loisa Curfman, Smith, Barrya F., 1997.
   Efficient management of parallelism in object oriented numerical software libraries.
   In: Arge, E., Bruaset, A.a M., Langtangen, H.a P. (Eds.), Modern Software Tools in Scientific Computing. Birkhäuser Press, pp. 163–202.
- Bensoussan, A., Lions, J.-L., Papanicolaou, G., 1978. Asymptotic analysis for periodic structures. North-Holland Pub. Co., p. 700.
- Borodulina, Svetlana, Kulachenko, Artem, Nygårds, Mikael, Galland, Sylvain, 2012. Stress-strain curve of paper revisited. Nordic Pulp Pap. Res. J. 27 (2), 318–328.
- Borodulina, S., Motamedian, H.R., Kulachenko, A., 2018. Effect of fiber and bond strength variations on the tensile stiffness and strength of fiber networks. Int. J. Solids Struct. 154, 19–32.
- Bosco, Emanuela, Peerlings, Rona H.J., Geers, Marca G.D., 2015. Predicting hygroelastic properties of paper sheets based on an idealized model of the underlying fibrous network. Int. J. Solids Struct. 56, 43–52.
- Bosco, E., Peerlings, R.H.J., Geers, M.G.D., 2016. Asymptotic homogenization of hygro-thermo-mechanical properties of fibrous networks.
- Bosco, E., Peerlings, R.H.J., Geers, M.G.D., 2017. Hygro-mechanical properties of paper fibrous networks through asymptotic homogenization and comparison with idealized models. Mech. Mater. 108, 11–20.
- Bosco, Emanuela, Peerlings, Rona H.J., Schoenmakers, Nouda P.T., Dave, Nik, Geers, Marca G.D., 2022. Hygro-mechanics of fibrous networks: A comparison between micro-scale modelling approaches. Elsevier, pp. 179–201,
- Chen, Xiaoming, Chen, Li, Zhang, Chunyan, Song, Leilei, Zhang, Diantang, 2016.
  Three-dimensional needle-punching for composites ? A review. Composites A 85, 12–30.
- Cheng, H., Zhu, X., Cheng, X., Cai, P., Liu, J., Yao, H., Zhang, L., Duan, J., 2023. Mechanical metamaterials made of freestanding quasi-BCC nanolattices of gold and copper with ultra-high energy absorption capacity. Nature Commun. 14 (1).
- Cox, Ha L, 1952. The elasticity and strength of paper and other fibrous materials. Br. J. Appl. Phys. 3 (3), 72–79.
- Cucumazzo, V., Demirci, E., Pourdeyhimi, B., Silberschmidt, V.V., 2021. Anisotropic mechanical behaviour of calendered nonwoven fabrics: Strain-rate dependency. J. Compos. Mater. 55 (13), 1783–1798.
- Cucumazzo, Vincenzo, Silberschmidt, Vadima V., 2022. Mechanical behaviour of nonwovens: Continuous approach with parametric finite-element modelling. 451, pp. 35–70,
- Dabiryan, H., Karimi, M., Varkiani, S.a Mohammada Hosseini, Nazeran, S., 2018. Simulating the structure and air permeability of needle-punched nonwoven layer. J. Text. Inst. 109 (8), 1016–1026.
- Farukh, Farukh, et al., 2013. Meso-scale deformation and damage in thermally bonded nonwovens. J. Mater. Sci. 48 (6), 2334–2345.
- Ganghoffer, Jeana François, Goda, Ibrahim, ElNady, Khaled, Rahali, Yosra, 2020.
  Prediction of the Effective Mechanical Properties of Regular and Random Fibrous Materials Based on the Mechanics of Generalized Continua. vol. 596, CISM International Centre for Mechanical Sciences, Courses and Lectures, pp. 63–122.
- Geers, M.G.D., Kouznetsova, V.G., Brekelmans, W.A.M., 2001. Gradient-enhanced computational homogenization for the micro-macro scale transition. J. Phys. IV Colloque 11 (5), 145–152.
- Geuzaine, Christophe, Remacle, Jean-François, 2009. Gmsh: A 3-D finite element mesh generator with built-in pre- and post-processing facilities. Internat. J. Numer. Methods Engrg. 79 (11), 1309–1331.
- Hashin, Z., Shtrikman, S., 1963. A variational approach to the theory of the elastic behaviour of multiphase materials. J. Mech. Phys. Solids 11 (2), 127–140.
- He, Bang, Schuler, Louis, Newell, Pania, 2020. A numerical-homogenization based phase-field fracture modeling of linear elastic heterogeneous porous media. Comput. Mater. Sci. 176, 109519.
- Hill, R., 1963. Elastic properties of reinforced solids: Some theoretical principles. J. Mech. Phys. Solids 11 (5), 357–372.

- Huet, C., 1990. Application of variational concepts to size effects in elastic heterogeneous bodies. J. Mech. Phys. Solids 38 (6), 813–841.
- Huet, Christian, 1999. Coupled size and boundary-condition effects in viscoelastic heterogeneous and composite bodies. Mech. Mater. 31 (12), 787–829.
- Ivanovich, Dimitrienkoa Yuriy, Sokolov, Alexandera Pavlovich, 2010. Metod konechnykh elementov dlja reshenia lokal'nykh zadach mekhaniki kompozitsionykh materialov [finite element method for solving local problems of mechanics of composite materials]. p. 66.
- Karakoc, Alp, Paltakari, Jouni, Taciroglu, Ertugrul, 2020. On the computational homogenization of three-dimensional fibrous materials. Compos. Struct. 242, 112151.
- Kouznetsova, Varvaraa Gennadyevna, 2002. Computational homogenization for the multi-scale analysis of multi-phase materials. ISBN: 9038627343.
- Kouznetsova, V.G., Geers, M.G.D., Brekelmans, W.A.M., 2004. Multi-scale second-order computational homogenization of multi-phase materials: a nested finite element solution strategy. Comput. Methods Appl. Mech. Eng. 193 (48–51), 5525–5550.
- Kulachenko, Artem, Uesaka, Tetsu, 2012. Direct simulations of fiber network deformation and failure. Mech. Mater. 51, 1–14.
- Kuts, M.S., Walker, J.T., 2023. Fibrous porous media homogenization. GitHub repository,
- Liu, Qiang, Lu, Zixing, Hu, Zijun, Li, Junning, 2013. Finite element analysis on tensile behaviour of 3D random fibrous materials: Model description and meso-level approach. Mater. Sci. Eng. A 587, 36–45.
- Liu, Q., Lu, Z., Zhu, M., Yang, Z., Hu, Z., Li, J., 2014. Experimental and FEM analysis of the compressive behavior of 3D random fibrous materials with bonded networks. J. Mater. Sci. 49 (3), 1386–1398.
- Lu, Zixing, Liu, Qiang, Han, Haitao, Zhang, Dahai, 2013. Experiment and modeling on the compressive behaviors for porous silicon nitride ceramics. Mater. Sci. Eng. A 559, 201–209.
- Mansour, Rami, Kulachenko, Artem, 2022. Stochastic constitutive model of thin fibre networks. Elsevier, pp. 75–112,
- Mansour, Rami, Kulachenko, Artem, Chen, Wei, Olsson, Mårten, 2019. Stochastic constitutive model of isotropic thin fiber networks based on stochastic volume elements. Materials 12 (3).
- Moulinec, H., Suquet, P., 1994. A fast numerical method for computing the linear and nonlinear mechanical properties of composites. C. R. Acad. Sci. Ser. II. Mec. Phys. Chim. Astronom..
- Ostoja-Starzewski, M., 2006. Material spatial randomness: From statistical to representative volume element. Probab. Eng. Mech. 21 (2), 112–132.
- Pahr, D.H., Böhm, H.J., 2008. Assessment of mixed uniform boundary conditions for predicting the mechanical behavior of elastic and inelastic discontinuously reinforced composites. 00, (0), pp. 1–12,
- Panasenko, G.P., 2008. Homogenization for periodic media: From microscale to macroscale. Phys. Atom. Nucl. 71 (4), 681–694.
- Picu, R.C., 2011. Mechanics of random fiber networks?a review. Soft Matter 7 (15), 6768-6785
- Pivovarov, D., Mergheim, J., Willner, K., Steinmann, P., 2022. Stochastic local FEM for computational homogenization of heterogeneous materials exhibiting large plastic deformations. Comput. Mech. 69 (2), 467–488.
- Pivovarov, D., Zabihyan, R., Mergheim, J., Willner, K., Steinmann, P., 2019. On periodic boundary conditions and ergodicity in computational homogenization of heterogeneous materials with random microstructure. Comput. Methods Appl. Mech. Engrg. 357.
- Pobedrya, B.E., 1983. Numerical solution of problems of the mechanics of a deformable solid inhomogeneous body. Vestnik Moskov. Univ. Ser. I Mat. Mekh. (4), 78–85.
- Rahali, Y., Goda, I., Ganghoffer, J.F., 2016. Numerical identification of classical and nonclassical moduli of 3D woven textiles and analysis of scale effects. Compos. Struct. 135, 122–139.
- Samantray, P., et al., 2022. Role of inter-fibre bonds and their influence on sheet scale behaviour of paper fibre networks. Int. J. Solids Struct. 256.
- Sánchez-Palencia, E., 1980. Non-Homogeneous Media and Vibration Theory. In: Lecture Note in Physics, vol. 320, Springer-Verlag, pp. 57–65.
- Scroggs, Matthewa W., Baratta, Igora A., Richardson, Chrisa N., Wells, Gartha N., 2022a. Basix: a runtime finite element basis evaluation library. J. Open Source Softw. 7 (73), 3982.
- Scroggs, Matthewa W., Dokken, Jørgena S., Richardson, Chrisa N., Wells, Gartha N., 2022b. Construction of arbitrary order finite element degree-of-freedom maps on polygonal and polyhedral cell meshes. ACM Trans. Math. Software 48 (2).
- Sozumert, E., Farukh, F., Demirci, E., Acar, M., Pourdeyhimi, B., Silberschmidt, V.V., 2015. Damage mechanisms of random fibrous networks. 628, (1), Institute of Physics Publishing,
- Sullivan, C. Bane, Kaszynski, Alexander, 2019. PyVista: 3D plotting and mesh analysis through a streamlined interface for the visualization toolkit (VTK). J. Open Source Softw. 4 (37), 1450.
- Vazic, Bozo, Abali, Bilena Emek, Newell, Pania, 2022b. Determining parameters in generalized thermomechanics for metamaterials by means of asymptotic homogenization. arXiv preprint arXiv:2207.03353.
- Vazic, B., Abali, B.E., Newell, P., 2023. Generalized thermo-mechanical framework for heterogeneous materials through asymptotic homogenization. Contin. Mech. Thermodyn. 35 (1), 159–181.

- Vazic, B., Abali, B.a E., Yang, H., Newell, P., 2022a. Mechanical analysis of heterogeneous materials with higher-order parameters. Eng. Comput. 38 (6), 5051–5067.
- Veyhl, C., Fiedler, T., Jehring, U., Andersen, O., Bernthaler, T., Belova, I.V., Murch, G.E., 2013. On the mechanical properties of sintered metallic fibre structures. Mater. Sci. Eng. A 562, 83–88.
- Walters, Davida J., Luscher, Darbya J., Yeager, Johna D., 2021. Considering computational speed vs. accuracy: Choosing appropriate mesoscale RVE boundary conditions. Comput. Methods Appl. Mech. Engrg. 374, 113572.
- Yilmaz, K.B., Sabuncuoglu, B., Yildirim, B., Silberschmidt, V.V., 2020. A brief review on the mechanical behavior of nonwoven fabrics. J. Eng. Fibers Fabrics 15.